Petroleum Science 23 (2026) 1360–1370

Contents lists available at ScienceDirect

Petroleum Science

journal homepage: www.keaipublishing.com/en/journals/petroleum-science

Original Paper

Large-scale physical simulation of flow behavior in Kelasu ultra-deep fractured low-porosity sandstone gas reservoirs

Yong-Liang Tang [a,b], Jun Yao [c,d], Xue-Hao Pei [a,*], Dong Chen [a,e], Yong-Bin Zhang [a,f], Feng-Lai Yang [a,e], Xu Zhou [c,d], Zhao-Qin Huang [c,d]

[a] Tarim Oilfield Company, PetroChina, Korla, 841000, Xinjiang, China
[b] School of Earth and Space Sciences, Peking University, Beijing, 100871, China
[c] National Key Laboratory of Deep Oil and Gas, China University of Petroleum (East China), Qingdao, 266000, Shandong, China
[d] School of Petroleum Engineering, China University of Petroleum (East China), Qingdao, 266000, Shandong, China
[e] R&D Center for Ultra-Deep Complex Reservoir Exploration and Development, CNPC, Korla, 841000, Xinjiang, China
[f] Xinjiang Key Laboratory of Ultra-deep Oil and Gas, Korla, 841000, Xinjiang, China

ARTICLE INFO

Article history:
Received 3 August 2025
Received in revised form
15 September 2025
Accepted 7 November 2025
Available online 17 November 2025

Edited by Meng-Jiao Zhou

Keywords:
Fractured low-porosity sandstone
Large-scale physical simulation
Multi-scale fractures
Gas-water two-phase flow

ABSTRACT

The ultra-deep fractured low-porosity sandstone gas reservoirs in the Kuqa Depression of the Tarim Basin exhibit complex characteristics, including high temperature, high pressure, significant in-situ stress, multi-scale fractures, and strong aquifer activity. The development of these reservoirs is challenged by rapid water invasion, which causes severe production declines. Conventional experiments fail to adequately simulate the coupled flow between the in-situ matrix and fractures. This study developed a high-temperature, high-pressure large-scale physical simulation platform and a methodology for preparing large rock samples with complex fractures. Using this platform, we conducted single-phase and gas-water two-phase flow experiments under in-situ conditions. The key results indicate that during single-phase depletion, cumulative gas production rapidly reaches a quasi-steady state, confirming the hierarchical flow and coupling from “large fracture” to “small fracture” to “matrix”. The matrix’s gas supply capacity diminishes with decreasing pressure, exacerbating the supply-production imbalance. Constant-volume bottom water experiments reveal that when fracture water saturation exceeds a critical threshold, the matrix gas supply abruptly declines due to “water-sealed gas”. Continuous fracture drainage and pressure reduction can partially alleviate this sealing and restore some gas supply, although recovery remains limited. Experiments under different management strategies demonstrate that higher production rates and larger water-to-gas volume ratios lead to lower cumulative gas production before water sealing, higher abandonment pressures, greater challenges in post-sealing recovery, and consequently, lower ultimate recovery. These findings provide critical insights for optimizing development strategies in ultra-deep fractured low-porosity sandstone gas reservoirs.

1. Introduction

The development of ultra-deep tight sandstone gas reservoirs represents a formidable challenge within the global oil and gas sector. These reservoirs are typically marked by multi-scale fracture development, and their fluid dynamics in porous media are governed by matrix-fracture interactions. The presence of active water bodies frequently leads to significant operational challenges, including a rapid decline in production following water breakthrough and highly unpredictable reservoir behavior. Consider the Kelasu gas field in the Kuqa depression of the Tarim Basin as an illustrative case. This field is among the few ultra-deep and ultra-high-pressure fractured low-porosity sandstone gas reservoirs in China. It has undergone numerous tectonic phases, resulting in a complex geological structure characterized by high

* Corresponding author.
E-mail address: peixh-tlm@petrochina.com.cn (X.-H. Pei).
Peer review under the responsibility of China University of Petroleum (Beijing).

https://doi.org/10.1016/j.petsci.2025.11.020

Nomenclature

g	Acceleration of gravity, m/s^2
K_f, K_m	Fracture, matrix permeability, μm^2
L	Characteristic length, m
p_c	Capillary force, Pa
Δp	Displacement pressure, Pa
q	Flow rate of production well, m^3/s
r_w	Well diameter, m
t	Production time, s
v_f	Flow velocity in the fracture, m/s
V	Apparent volume of the model, m^3
V_{pf}	Fracture pore volume, m^3
V_{pm}	Matrix pore volume, m^3
x, y, z	Coordinates of any point in the study area, m
μ_g, μ_w	Viscosity of gas and water, mPa·s
μ	Average viscosity of fluid, mPa·s
ρ_g, ρ_w	Density of gas and water, kg/m^3
ρ	Average density of fluid, kg/m^3
ϕ	Total porosity of the model
ϕ_m	Matrix porosity

steepness at the surface and overthrust faults. The reservoir is buried at depths reaching up to 8,271 m, with an average depth of 6,850 m, and exhibits low matrix porosity (4%–8%) and permeability (0.04–1 mD). It is typified by "three highs and two strong characteristics": formation temperatures of 100–190 °C, reservoir pressures of 80–140 MPa, in-situ stresses of 100–180 MPa, pronounced heterogeneity in multi-scale fracture development, and the presence of active water bodies. On one hand, the presence of natural fractures significantly enhances the physical properties of ultra-low-permeability sandstone reservoirs, thus serving as the primary conduits for oil and gas migration, which underpins the high productivity of gas wells. On the other hand, the efficient transport of water through these fractures leads to rapid water encroachment at the well bottoms during production, precipitating a marked decline in output and adversely affecting the stability of gas well production. The tight matrix and fractures together form a multi-scale medium with a discontinuous distribution, where the permeability contrast may span 5–6 orders of magnitude. The flow mechanisms and patterns differ across these media, and their distribution laws critically influence the coupled flow between media, ultimately impacting production dynamics.

Dynamic monitoring results have revealed significant disparities in productivity between wells, rapid pressure responses, and non-uniform rates of water invasion. To address these issues, researchers have introduced a novel reservoir classification termed the "pore–fracture–fault" triple multi-scale media (Wei et al., 2019). They employed discrete characterization methods to delineate the flow dynamics across various porous media within multi-scale fracture and fault systems. This preliminary investigation elucidated the dynamic behaviors of "coupling synergistic gas supply, water channeling-induced gas isolation, and sealing" in gas reservoirs under diverse fracture network development modes. This methodology has enhanced the prediction accuracy of gas-water transport and the distribution of residual gas within these reservoirs. Nevertheless, it has not yet satisfied the demands for fine-scale development. Further investigations into multi-scale flow in porous media, through experiments and mechanism studies under in-situ high-temperature and high-pressure conditions, are essential to promote the efficient exploitation of ultra-deep gas reservoirs.

Extensive research has been conducted globally on matrix-fracture coupled flow in porous media through physical simulation experiments. Predominantly, these studies have concentrated on pore-scale 2D microsimulations (Shoukry et al., 2023), Plexiglas-based physical simulations of fracture-vug reservoirs in carbonate formations (Zhao et al., 2020), NMR or CT-based plunger experiments (Tang et al., 2017), and physical simulations utilizing full-diameter cores or sand-filled tubes (Wang et al., 2017), as well as two-dimensional and three-dimensional physical simulations employing large-scale sand filling or rock plate fracture creation (Chen et al., 2024). Pore-scale two-dimensional microscopic models typically utilize materials such as silicon wafers, glass, or actual sandstone thin sections to visually demonstrate fluid exchange processes between the matrix and fractures at the pore level (Zhong et al., 2018; Ahmadi et al., 2019; Du et al., 2020). Nevertheless, the limited size of these models constraints the scale of fractures, making it challenging to accurately represent the spatial relationship between matrix and fracture reservoir spaces. The Plexiglas-based physical simulation technique for fracture-vug reservoirs primarily facilitates the simulation of such reservoirs in carbonate rocks, where matrix pores are negligible (Wang et al., 2022, 2024; Sun et al., 2022; Li et al., 2012), rendering it unsuitable for fractured low-porosity sandstone gas reservoirs. The small diameter of core plunger samples results in a disproportionately high fluid penetration depth from fractures into the matrix, thereby yielding an experimentally measured waterflood sweep efficiency that exceeds actual reservoir conditions. The physical simulation method using full-diameter cores or sand-filled tubes, supported by advanced experimental apparatus, enables the construction of diverse flow media combinations through naturally fractured cores (Liu et al., 2021; Fang et al., 2019), artificially fractured cores (Shen et al., 2014; Huang et al., 2019), or multiple cores in a series-parallel configuration (Hu et al., 2022; Xu et al., 2020). This approach is currently the predominant method for conducting high-temperature and high-pressure gas reservoir flow experiments (Yang et al., 2024). However, limitations in core size impede the construction of intricate multi-scale fracture networks.

Additionally, conventional core experiments primarily capture end-face production data, failing to observe dynamic parameters such as internal pressure distributions. In contrast, two-dimensional and three-dimensional physical simulations, which utilize large-scale sand filling or rock plate fracture creation, overcome the limitations inherent in indoor experiments like conventional plunger, full-diameter, and microscopic scanning. These indoor methods often struggle to characterize multi-scale fracture flow accurately. The aforementioned simulations facilitate a crucial transition from centimeter to meter scales, serving as an essential link between core-scale and reservoir-scale studies. They significantly mitigate uncertainties related to scale-up in unified modeling and numerical simulation, offering substantial advantages. Consequently, numerous scholars have pursued this methodological approach (Fang et al., 2016, 2024; Tong et al., 2015; Liu et al., 2023; Ge et al., 2018). The flexible design of fracture distributions is achievable through techniques such as sand filling or rock plate fracture creation, which have been widely applied in reservoir waterflood simulations. However, due to their large scale and the limitations of experimental apparatuses, these models are typically sealed with epoxy resin without external confining pressure support and are subjected to direct testing. Their pressure resistance generally remains below 1 MPa (Fang et al., 2016; Guo et al., 2011; Li et al., 2021; Zheng et al., 2017; Tong et al., 2015; Liu et al., 2013). Through ongoing enhancements to the experimental apparatus platform, the pressure in two-dimensional large-scale simulations has reached 70 MPa (Liu et al., 2023; Guo

et al., 2024), while the pressure in three-dimensional large-scale simulations remains within 20 MPa (Ge et al., 2018). These pressures are insufficient to simulate the production processes of ultra-deep, high-temperature, and high-pressure gas reservoirs with complex multi-scale fractures under in-situ conditions. This limitation restricts the study of flow mechanisms in porous media within ultra-deep fractured low-porosity sandstone gas reservoirs.

This paper focuses on the ultra-deep fractured low-porosity sandstone gas reservoir in the Tarim Basin, using typical outcrop rock samples to establish a large-scale three-dimensional physical model. This model characterizes the integration of matrix pores and multi-scale fractures, with reference to the prevalent fracture development modes in gas reservoirs. Additionally, a complementary high-temperature and high-pressure in-situ experimental platform has been developed to conduct simulation experiments on fractured water-bearing gas reservoirs. These experiments are designed to investigate the water intrusion mechanism in such reservoirs, identify influencing factors, and analyze recovery efficiency characteristics under various development strategies. The findings provide a theoretical basis to inform the formulation of sound technical development policies for fractured low-porosity sandstone gas reservoirs.

2. Experimental methods

The significant permeability contrast between the matrix and the multi-scale fractures/faults in fractured, low-porosity sandstone gas reservoirs engenders complex flow behaviors of gas and water. This presents a quintessential multi-scale flow problem. The reservoir comprises multi-scale media including micro/nano-scale pores, micro-fractures, faults, and complex networks of natural and artificial fractures, which are distributed discontinuously. A critical aspect of understanding the flow mechanisms within such multi-scale media is the construction of multi-scale fractures.

2.1. Similarity principle

Marked differences in scale and the physical properties of fluids exist between conditions in fractured, low-porosity sandstone gas reservoirs under natural reservoir conditions and those recreated in laboratory settings. To accurately simulate the flow of reservoir fluids under experimental conditions, it is imperative to maintain fixed ratios of corresponding physical quantities across the two flow fields. Consequently, this study employs the similarity principle to guide both the construction of the experimental model and the selection of test fluids. This approach integrates the analysis of governing equations and dimensional analysis, from which a set of similarity criteria has been established. Following simplification, 13 similarity criteria were derived to inform the design of experimental parameters, as detailed in Table 1.

The actual gas reservoir simulated in this study is characterized as an edge-water gas reservoir with near-bottom water, originally at a formation pressure of 106 MPa. During depletion production, as pressure decreases to approximately 70 MPa, wells positioned at lower perforated intervals along the reservoir margin begin to experience water breakthrough. At this juncture, the state of the water within the reservoir transitions to bottom water. Consequently, the model employs the state of the reservoir at 70 MPa as the initial state for the simulation. A local rectangular domain, situated between the bottom of the well and the bottom water, is selected to investigate the process of water intrusion from the bottom upwards into the gas reservoir. The specific parameters of both the prototype gas reservoir and the physical model are presented in Table 2.

2.2. Multi-scale fracture modelling design and fabrication

The designated gas reservoir exhibits well-developed fractures, encompassing faults and other fracture types with apertures reaching up to the millimeter scale, as well as finer fractures possessing apertures on the micrometer scale. The predominant orientation of these fractures is a dip angle ranging from 60° to 85°. To effectively simulate the dissecting impact of this medium-to-high angled fracture network on the matrix blocks, and given the challenges associated with cutting rock samples, the fracture network depicted in Fig. 1(a) is strategically comprised of both horizontal and vertical fractures. This configuration includes two horizontal fractures and diagonal vertical fractures, classified as large-scale fractures with an aperture of 1 mm, and cross vertical fractures aligned parallel to the model's edges, classified as small-scale fractures with an aperture of 0.1 mm. The production well is strategically located at the upper corner of the model, intersecting a large-scale fracture. Four pressure gauging points have been installed at the centers of four matrix blocks within the upper and lower sections of the model, positioned at varying proximities from the production well. The model also integrates a bottom water inlet, manifested as a small-scale fracture at the base of the model, Fig. 1(a).

The model preparation process, as illustrated in Fig. 1(b), begins with the cutting of natural rock samples utilizing wire-cutting equipment designed for precision (achieving an accuracy of $\pm$0.01 mm to ensure the flatness of the fracture surfaces). Following this, the three-dimensional large-scale fractured rock samples are manually assembled. For matrix blocks that are equipped with pressure measurement points, holes are drilled to extend into the center of each block. A 3 mm pressure tubing is subsequently inserted into these holes, and epoxy resin is used to seal the annulus between the tubing and the block, with the exception of the tubing ports. Additionally, for both the production wells and the bottom water inlets, a shallow slot is directly machined on the fracture surface to house the 3 mm tubing. After routing the model's pressure and fluid injection-production tubing to a single side, the assembly is placed into a mold and encapsulated with high-temperature-high-pressure epoxy resin. Upon curing, the mold is removed to reveal the finalized model. This method offers several advantages over traditional multi-scale fracture model fabrication techniques, including improved resistance to high temperatures and pressures, enhanced similitude to actual gas reservoir conditions, and the ability to control multi-scale fracture apertures precisely.

The large-scale fractures are fortified with ceramic proppant (0.85 ± 0.02 mm), as depicted in Fig. 1(c). The ceramic proppant is initially spread upon a viscous porous film to create an easily manageable proppant sheet, which is subsequently positioned within the large-scale fractures according to predetermined placements during the assembly process.

2.3. Experimental apparatus

In this study, we constructed an experimental setup tailored to the requirements of large-scale physical modeling under high-temperature and high-pressure conditions, as depicted in Fig. 2. The setup comprises three main components: a high-temperature and high-pressure injection system for large-scale rock samples, a high-temperature and high-pressure experimental chamber, and a data collection system. The injection system consists of an advection pump, an intermediate vessel, and a large-capacity

Table 1
Main similarity criteria and their physical significance.

Similar condition	Similarity criterion	Physical significance
Geometric similarity	$\pi_1 = x/L$	Dimensionless x-direction spatial position
	$\pi_2 = y/L$	Dimensionless y-direction spatial position
	$\pi_3 = z/L$	Dimensionless z-direction spatial position
	$\pi_4 = r_w/L$	Ratio of wellbore radius to characteristic length
Dynamic similarity	$\pi_5 = \mu_g/\mu_w$	Viscosity ratio
	$\pi_6 = \rho_g/\rho_w$	Density ratio
	$\pi_7 = \rho g L/\Delta p$	Ratio of gravity to displacement pressure
	$\pi_8 = p_c/\Delta p$	Ratio of capillary force to displacement pressure
Kinematic similarity	$\pi_9 = V_{pf}/V_{pm}$	Ratio of fracture to matrix pore volume
	$\pi_{10} = \phi_m$	Matrix porosity
	$\pi_{11} = K_f/K_m$	Ratio of fracture to matrix permeability
	$\pi_{12} = \rho v_f L/\mu$	Ratio of inertial force to viscous force
	$\pi_{13} = qt/(V\phi)$	Dimensionless time

Table 2
Main physical parameters.

Parameter type	Gas reservoir prototype	Physical model	Scale factor
Fluid medium	Formation water, natural gas	Pure water, nitrogen	–
L_x, L_y, L_z	100 m, 100 m, 100 m	26 cm/26 cm/26 cm	384.6
Pressure	77 MPa	70 MPa	1
Gas-water viscosity ratio	0.031 mPa s/0.3 mPa s	0.04 mPa s/0.41 mPa s	1.06
Gas-water density ratio	371 kg/m^3/1079 kg/m^3	443.6 kg/m^3/1006 kg/m^3	0.78
Temperature	152 °C	70 °C	2.17
Caliper	0.12 m	0.5 cm	24
Small scale fracture opening	0.1 mm	0.1 mm	1
Large-scale fracture (fault) opening	1 mm	1 mm	1
Matrix permeability	0.4 mD	0.4 mD	1
Matrix porosity	0.05	0.055	0.91
Production time	5 a	400 min	6570
Flow rate	50×10^4 m^3/d	600 mL/min	578704

bottom water reservoir. The high-temperature and high-pressure experimental chamber, illustrated in Fig. 3, includes a pressure-resistant shell, a confining pressure chamber, and an array of sealing mechanisms. Additionally, the chamber is equipped with capabilities for mechanical loading in the X- and Z-directions. However, the current study does not explore the effects of stress; therefore, these loading functions are not activated during the experiments. Upon placement of the model within the confining pressure chamber, it is entirely filled with a confining pressure fluid. This setup not only ensures a uniform pressure distribution around the exterior of the model but also utilizes the fluid as a heating medium to precisely control the model's temperature via cyclic heating. The collection system features a dynamic tracking pressure relief valve, a gas-liquid separation device, and a comprehensive data acquisition system. Through meticulous sealing procedures, the experiment maintains a maximum injection pressure of 80 MPa. For safety, the experimental design incorporates a maximum allowable pressure of 70 MPa.

2.4. Experimental content

Experiments focusing on single-phase gas depletion production were conducted alongside physical experiments investigating water invasion under conditions of fixed-volume water body depletion production, varying gas production rates, and differing water body multiples. The comprehensive experimental plan is delineated in Table 3, and the experimental procedures are as follows:

① The confining pressure chamber of the experimental apparatus was removed from the pressure hull, and the model was positioned within the confining pressure chamber. Following the connection of the experimental pipelines, the confining pressure chamber was reinserted into the pressure hull, and the confining pressure fluid loading apparatus was activated. Once the confining pressure fluid had filled the chamber, the exhaust port was sealed. An initial confining pressure of 5 MPa was applied; subsequently, the confining pressure fluid was circulated and heated to reach the desired experimental temperature.

② Both the model's bottom water inlet and the production well outlet were simultaneously evacuated. Subsequently, the bottom water inlet and the outlet of the production well were connected to the upper part of the piston of the gas injection intermediate vessel, which had a volume of 5 L and was pressurized to 2 MPa (at this juncture, the piston of the gas injection intermediate vessel was at its lowest position, and the bottom valve was sealed). This configuration was maintained until the pressures at the four pressure measurement points within the rock sample matrix and the pressure in the gas injection intermediate vessel stabilized and aligned.

③ The valve between the gas injection intermediate vessel and the model was sealed. The pressure boosting system was then connected and pressurized to 7 MPa, and the confining pressure was raised to 10 MPa. Upon reopening the valve between the gas injection intermediate vessel and the model, the pressures at the four pressure measurement points in the rock sample matrix and in the gas injection intermediate vessel were allowed to stabilize and align. Subsequently, the confining pressure and the pressure in the gas injection intermediate vessel were incrementally increased in 5 MPa steps during the gas injection into the model. This process continued until the pore pressure

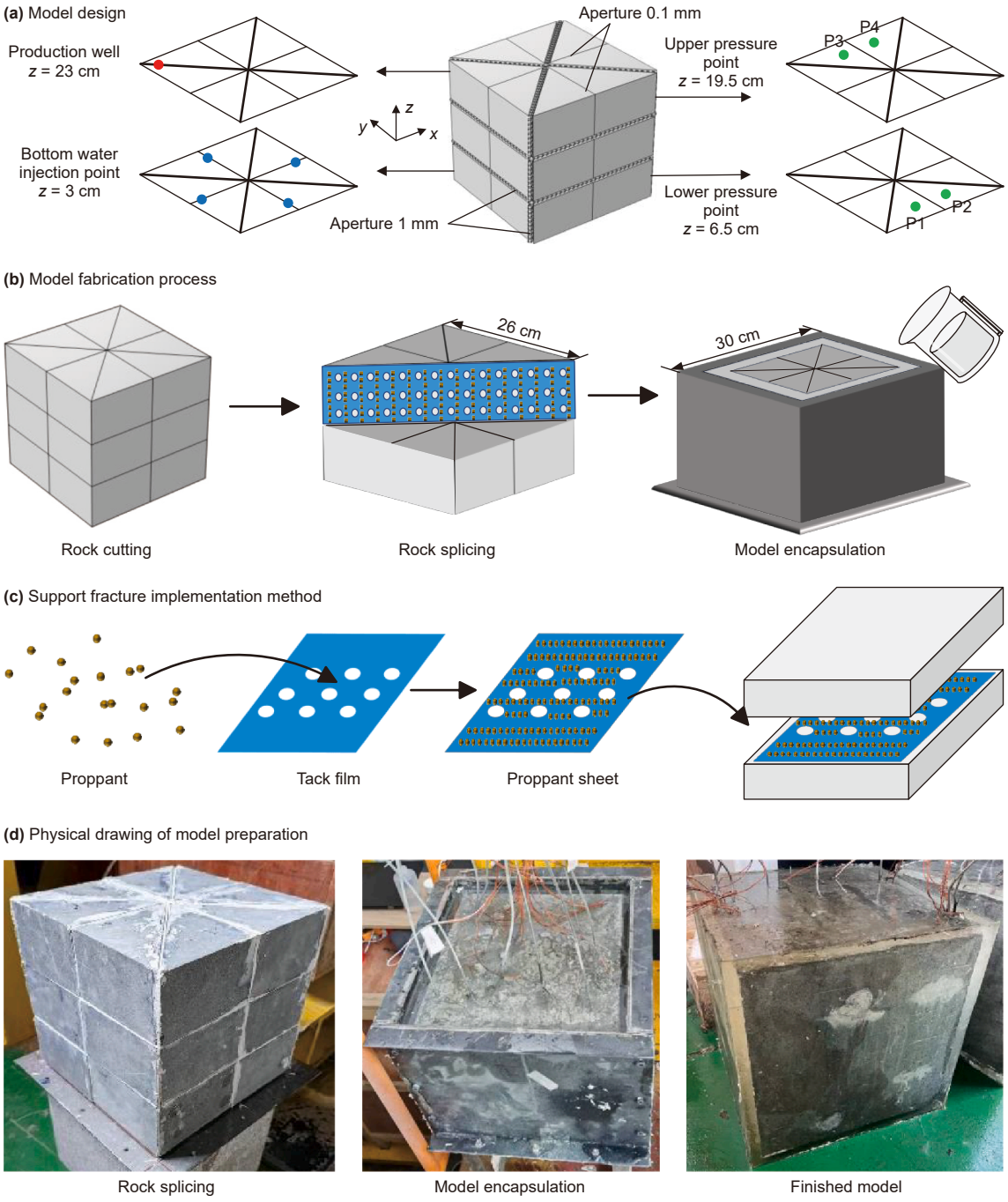

Fig. 1. Preparation of multi-scale fracture rock sample.

neared 60 MPa, at which point the lower part of the piston in the gas injection intermediate vessel was directly connected to the two-stage pressurization displacement pump. Water was then injected into the lower part of the piston to drive the gas from the gas injection intermediate vessel into the model, continuing until the pressures at all four pressure measurement points in the rock sample matrix reached 70 MPa, at which point saturation was terminated.

④ During the single-phase gas depletion production experiment, the inlet valve connected to the bottom water was sealed. In contrast, for the fixed-volume water body depletion experiment, the bottom water inlet pipeline was linked to a fixed-volume water body maintained at 70 MPa. Concurrently, the production well's outlet pipeline was connected to a computer-controlled tracking back-pressure valve. The pressure exerted by the back-pressure valve was incrementally reduced at a predetermined rate. Measurements were taken of both gas and water yields at the outlet, as well as the pressures at the various monitoring points located at the bottom water's end, the outlet, and within the experimental model itself. This experiment was concluded once the pressure at the outlet reached atmospheric levels.

⑤ The confining pressure was relieved, the fluid maintaining this pressure was evacuated, and the rock sample was replaced for the repetition of the aforementioned steps.

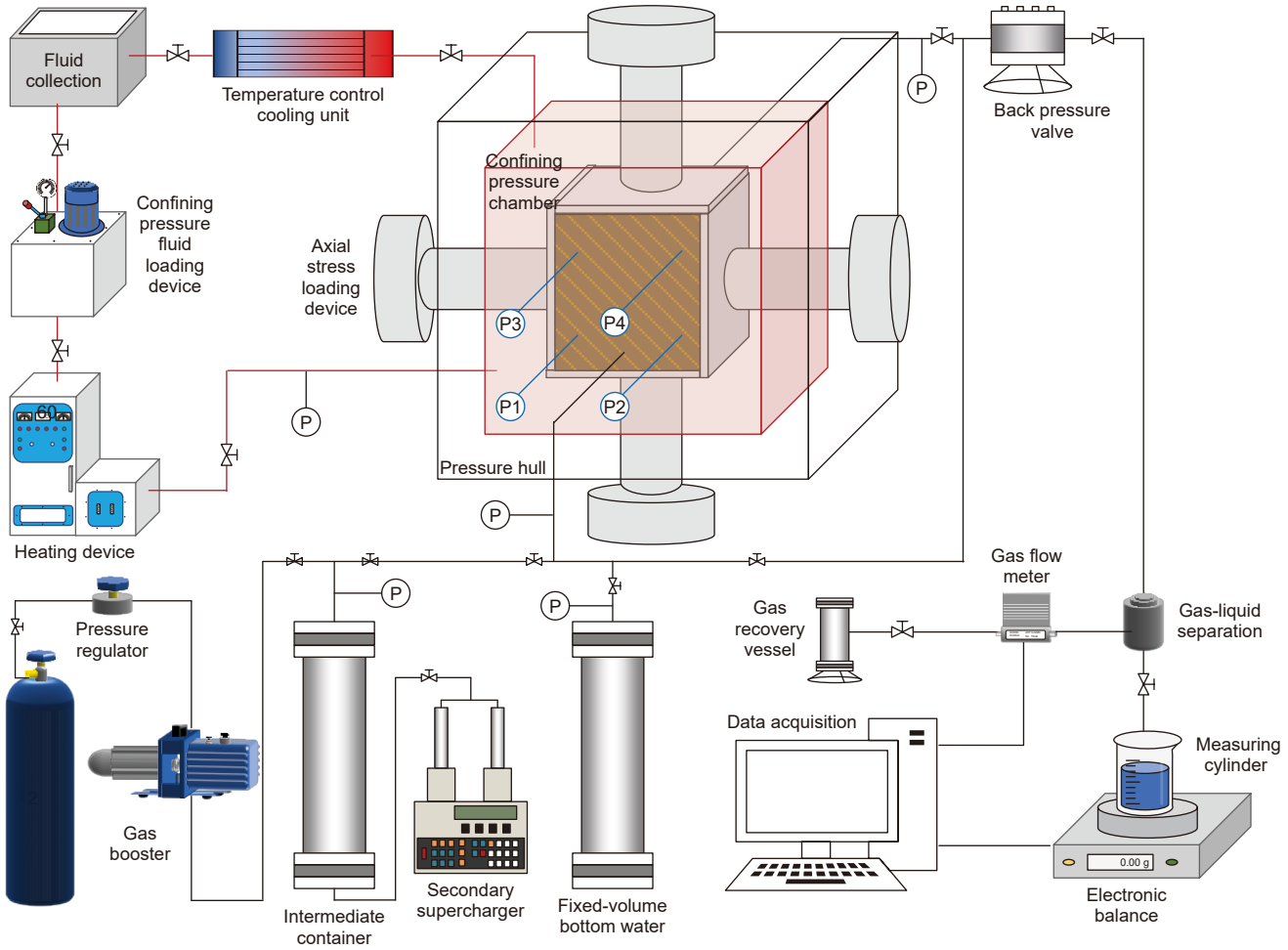

Fig. 2. Large scale physical simulation experiment flow chart.

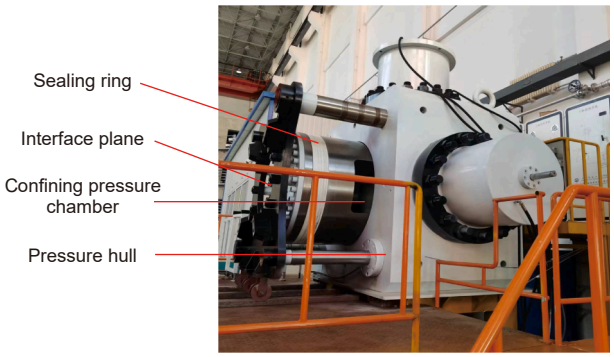

Fig. 3. High temperature and high pressure experimental chamber.

3. Experimental results

3.1. Results of single-phase gas depletion production

The production rates of wells during depletion and the corresponding pressure characteristics of the model are depicted in Fig. 4. Initially, gas from large fractures is produced first, followed by gas supply from the surrounding matrix of these fractures. Over time, smaller fractures and the entire matrix begin to contribute to the gas production. As the reserves being mobilized increase, the slope of the cumulative gas production curve steepens, reaching a pseudo-steady state rapidly. In this phase, the cumulative gas production curve increases linearly until nearing depletion, at which point the production rate declines due to a diminishing gas supply.

Both Fig. 4(a) and (b) demonstrate that the pressures in the matrix and fractures decrease almost synchronously in the early stages of the pressure drop, but they begin to diverge as the process progresses. This divergence is attributed to the combined effects of gas compression characteristics and the delayed gas supply from the matrix. The higher the gas pressure, the smaller the volume of gas expansion per unit of pressure drop. As the gas pressure decreases, the volume of gas expansion per unit of pressure drop increases, as illustrated in Fig. 5. Initially, when the pressure is high, the matrix only needs to release a small amount of high-pressure gas into the fractures to synchronize the pressure decline with that in the fractures. In the middle and late stages of production, as the pressure decreases, the volume of gas (at formation conditions) that needs to be released from the matrix for a unit pressure drop increases significantly. If the gas flow rate, driven by the pressure difference between the matrix and the fractures, is insufficient to release enough gas in a timely manner, it results in a lag in the matrix gas supply. Consequently, the pressure decline in the matrix slows down and diverges from that of the fracture pressure drop.

Table 3
Table of experimental programme.

Serial number	Experimental content
1	Initially, the model is saturated with single-phase gas at 70 MPa. Subsequently, the inlet is sealed and the production well is operated at a depletion rate of 10 MPa/h.
2	Initially, the model is saturated with single-phase gas at 70 MPa. Subsequently, the inlet is sealed and the production well is operated at a depletion rate of 15 MPa/h.
3	Initially, the model is saturated with single-phase gas at 70 MPa. The inlet is then connected to a 10 L constant-volume reservoir of bottom water, and the production well is operated at a depletion rate of 10 MPa/h.
4	Initially, the model is saturated with single-phase gas at 70 MPa. The inlet is then connected to a 10 L constant-volume reservoir of bottom water, and the production well is operated at a depletion rate of 15 MPa/h.
5	Initially, the model is saturated with single-phase gas at 70 MPa. The inlet is then connected to a 20 L constant-volume reservoir of bottom water, and the production well is operated at a depletion rate of 10 MPa/h.

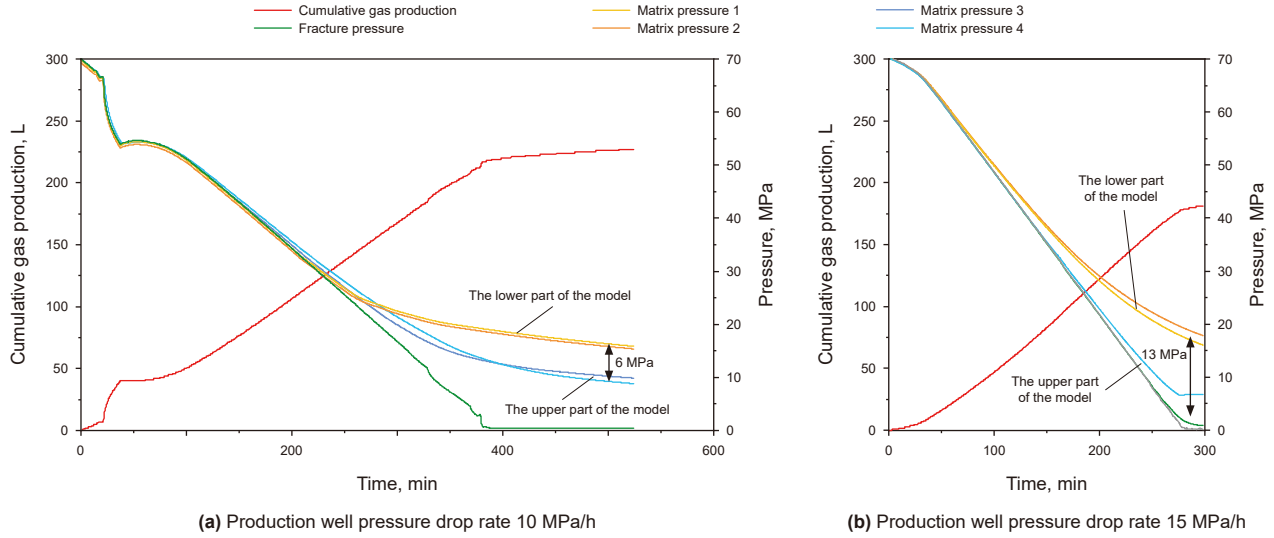

Fig. 4. Cumulative gas production and matrix pressure measurement points curves during single-phase gas depletion production.

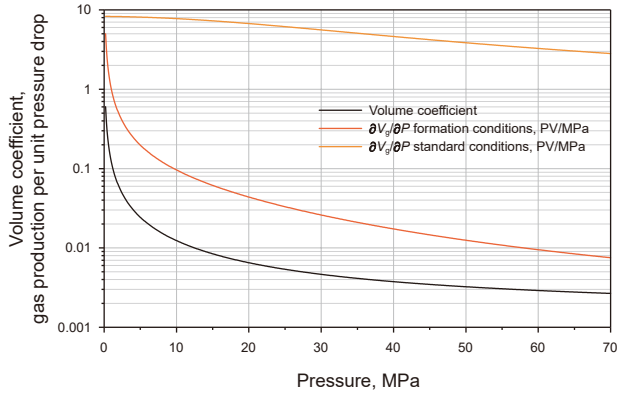

Fig. 5. Isothermal compression characteristic curve of nitrogen at 70 °C. V_g is the volume of gas expansion, and P is the pressure.

The observed phenomenon of pressure drop separation between the matrix and fractures indicates that the material exchange capacity between these two is limited. As the gas reservoir pressure declines, the standard condition volume of gas that can be discharged from the matrix into the fractures for the same formation volume significantly decreases. Therefore, from the perspective of surface production capacity, the matrix gas supply capability will substantially decline in the middle and late production stages. If production allocation is not adjusted during actual production, it could exacerbate the imbalance between supply and production, leading to a depletion of the fracture pressure and consequently causing abnormally intense water channeling.

The comparison of Fig. 4(a) and (b) reveals differences in matrix pressure between the upper and lower parts of the model, primarily due to temporal and spatial variations in flow. The production well is situated in the upper part of the model. Here, the pressure drop first affects the upper fracture system, causing a rapid decline in pressure in the upper fractures that then propagates downward through the fracture network. Due to its proximity to the production well, the upper matrix is directly exposed to the rapidly declining fracture pressure, prompting earlier gas flow from the matrix. Conversely, the pressure decline in the lower fractures lags behind. Coupled with the gas supply from the middle and upper matrix, this results in higher pressure in the lower fractures compared to those near the production well and a slower decline in matrix pressure. The faster the gas production rate, the greater the pressure gradient across the fractures, leading to a larger pressure difference between the upper and lower matrix blocks. Consequently, a higher proportion of gas production originates from the upper matrix blocks, leading to lower cumulative gas production. This phenomenon suggests that, even in the absence of water invasion, the remaining gas in actual gas reservoirs is predominantly located in the lower parts of the reservoir.

Moreover, the cumulative gas production curve depicted in Fig. 4 exhibits approximately linear growth before reaching

depletion, indicating that the gas production rate remains balanced during the uniform pressure drop at the production well. This observation supports the conclusion that the fractures within the model do not undergo closure under the experimental pressure.

3.2. Results of the fixed-volume bottom water depletion production

When analyzing a fixed-volume bottom water of 10 L (which is 8.7 times the reservoir volume), the production well operates with a pressure drop rate of 10 MPa/h. The characteristics of production, such as rate and model pressure, are depicted in Fig. 6. Fig. 6 illustrates that the production profile under the influence of bottom water exhibits distinct phases. These include the large fractures and surrounding matrix gas supply stage, the stable gas supply stage from both large and small fractures along with the matrix, the matrix water sealing stage, and the matrix water sealing recovery stage.

During the initial stage involving large fractures and the surrounding matrix, the reserves within the large fractures are the first to be mobilized, followed by a gradual gas supply from the matrix near these large fractures. As the pressure decreases to a critical threshold, the small fractures become active, transitioning the system into a stage where both large and small fractures, along with the matrix, stably supply gas. The slope of the cumulative gas production curve at this stage shows an increase compared to the previous stage.

As the overall pressure within the model decreases, the fixed-volume bottom water expands due to elastic energy. The volume of water expansion, calculated from the measured bottom water pressure and water compressibility coefficient (determined by directly depressurizing the water body and draining it into a measuring cylinder), is illustrated in the water expansion volume curve in Fig. 6(c). The water volume within the model represents the difference between the water expansion volume and the cumulative volume of water produced at the outlet. Initially, during the stage of gas supply from the large fractures and surrounding matrix, the pressure drop does not extend to the bottom water. However, when the small fractures become mobilized, the pressure drop reaches the bottom water, causing it to intrude into the fractures. This intrusion results in a noticeable step at the transition between Stage I and Stage II in the cumulative gas production curve, Fig. 6(c).

As the pressure declines, the bottom water continues to expand and the volume of water entering the model fractures gradually increases. When the water volume in the fractures reaches a certain threshold, the gas production rate sharply declines, causing the cumulative gas production curve to flatten. The fracture pressure continues to drop while the matrix pressure stabilizes, coinciding with water breakthrough in the production well (Stage III). This phenomenon occurs because once the fractures are flooded, the water from the fractures invades the matrix under the influence of capillary forces. This results in the formation of a resistance layer saturated with gas and water in the outer layer of the matrix near the fractures. This layer impedes the flow of gas from the matrix into the fractures, a process known as water sealing.

During the water sealing stage, the gas within the matrix is unable to penetrate the resistance layer to reach the fractures,

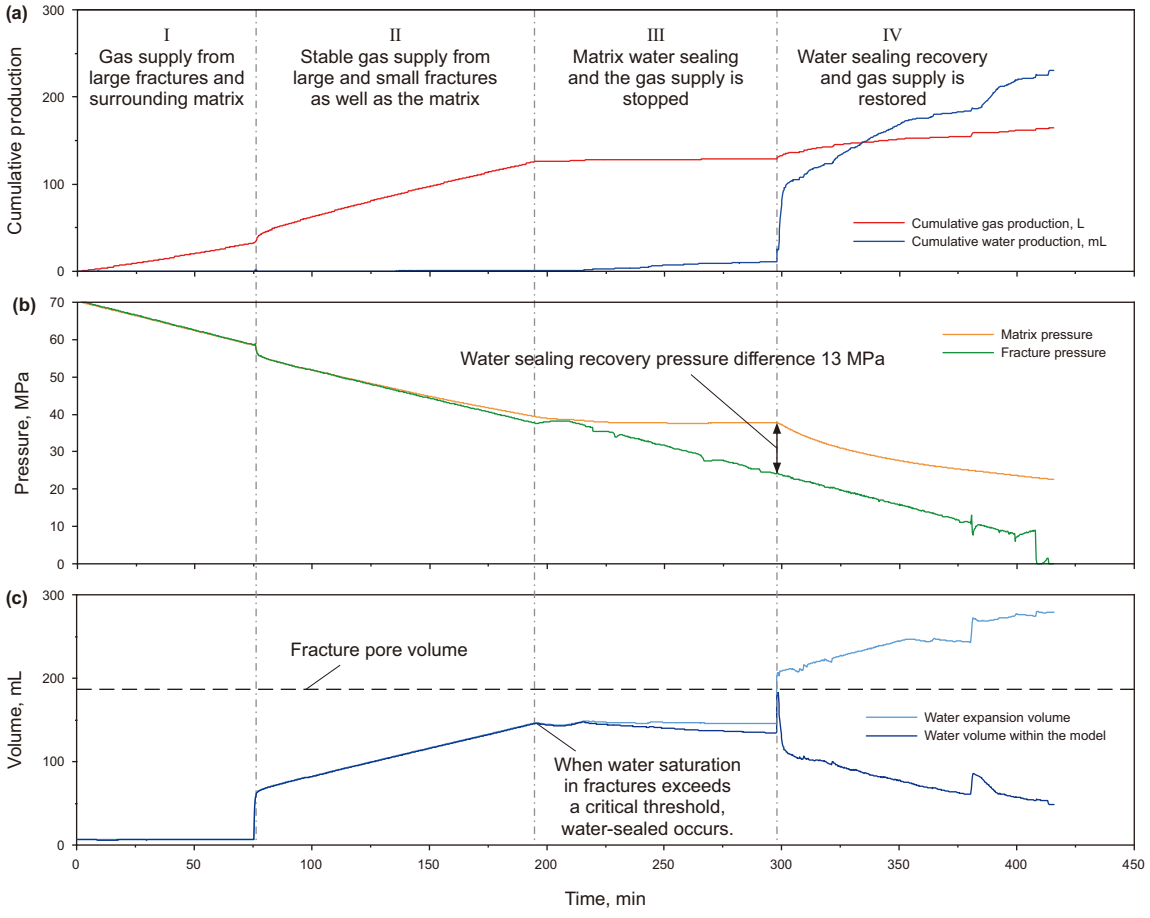

Fig. 6. Experimental results of fixed-volume water body depletion production.

causing the matrix pressure to remain stable. Meanwhile, the fracture pressure continues to drop due to the ongoing pressure decline in the production well. When the pressure differential between the matrix and the fractures reaches a specific threshold, the matrix pressure begins to decrease, signifying that gas supply from the matrix has resumed. We define this pressure threshold as the water sealing recovery pressure difference, which is depicted in Fig. 6 as 13 MPa.

Following the water sealing recovery in the matrix, gas supply is reestablished, marking the onset of Stage IV. In this stage, cumulative gas production starts to rise slowly. Concurrently, the rate at which bottom water is produced significantly increases compared to that in Stage III. However, due to the exceedingly high gas-water ratio during this stage, it may not present significant economic value for actual gas reservoir production.

3.3. Results of fixed-volume bottom water depletion production under different production methods

Experimental results for various gas production rates under a consistent water body multiple are presented in Fig. 7. These results show that an increased gas production rate leads to a quicker decline in both matrix and fracture pressures, higher matrix pressure at the onset of water sealing, and lower recovery efficiency upon water sealing. The primary cause of these outcomes is that a higher gas production rate widens the gap between gas supply from the matrix and gas extraction from fractures. This gap is compensated only by the elastic energy stored in the fracture reserves and the displacement effect caused by bottom water invading the fractures. Consequently, a faster gas production rate results in a greater volume of bottom water invasion per unit of pressure drop, which in turn leads to higher matrix pressure when complete water flooding in fractures results in water sealing.

Furthermore, Fig. 7 also reveals that a higher gas production rate increases the difficulty of recovering the matrix after water sealing. Therefore, in actual gas reservoir management, it is crucial to maintain a reasonable gas production rate to prevent premature water sealing of the reservoir, as this would significantly complicate enhanced gas recovery efforts.

Experimental results comparing the same gas production rate across different water body multiples are depicted in Fig. 8. These results demonstrate that a larger water body multiple results in higher matrix pressure at water sealing, lower recovery efficiency at water sealing, and increased difficulty in post-water-sealing matrix recovery. This trend is similar to the one observed with varying gas production rates. A larger water body multiple leads to greater bottom water invasion per unit pressure drop, accelerating water flooding and resulting in higher matrix pressure when complete water flooding in fractures triggers water sealing. Thus, in actual gas reservoir operations, managing a smaller gas production rate becomes essential with larger water body multiples to avoid premature water sealing of the reservoir.

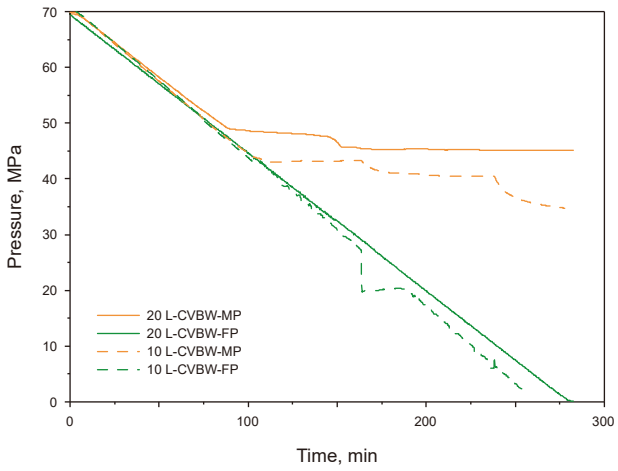

Fig. 8. Matrix and fracture pressures curves at different water body multiples.

4. Conclusion

(1) This study has innovatively established a method for preparing multi-level complex fracture flow media and has constructed a three-dimensional model that characterizes the combination of matrix pores and multi-scale fractures in ultra-deep fractured low-porosity sandstone gas reservoirs of the Tarim Basin. This model enables accurate characterization of large-scale and complex fractures.

(2) The independently developed large-scale high-temperature and high-pressure physical simulation experimental

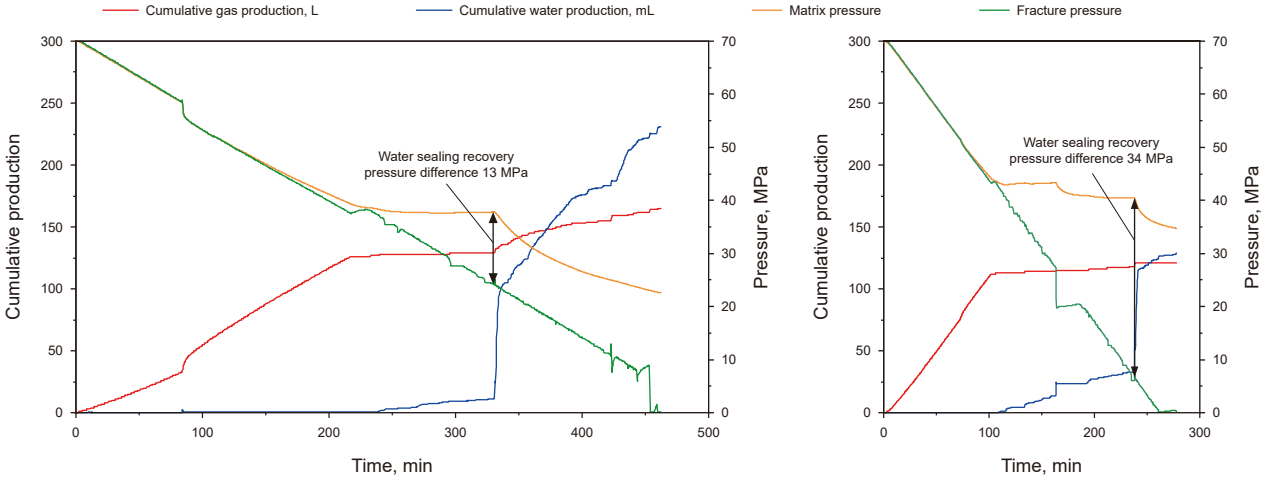

(a) Production well pressure drop rate 10 MPa/h

(b) Production well pressure drop rate 15 MPa/h

Fig. 7. Cumulative gas production, matrix and fracture pressures curves at different gas production rates.

platform, which can withstand pressures up to 80 MPa, has facilitated laboratory simulations of gas-water two-phase coupled flow processes in the matrix and multi-scale fractures under the in-situ conditions of ultra-deep gas reservoirs.

(3) Utilizing the three-dimensional large-scale physical simulation experimental platform and flow testing methods, we conducted depletion production simulations of fractured low-porosity sandstone gas reservoirs. The results indicate that during single-phase gas depletion production, gas initially emerges from large fractures, followed by gas from the adjacent matrix, and then gradually from smaller fractures and the entire matrix. The cumulative gas production curve's slope increases steadily and reaches a pseudo-steady state quickly. The experiments have confirmed the hierarchical mobilization and coupled superposition flow characteristics of "large fractures–small fractures–matrix" during production. Additionally, the observed phenomenon of pressure drop separation between the matrix and fractures in later production stages signifies a significant decline in matrix gas supply capacity. If production allocation remains unadjusted in actual operations, it can exacerbate the supply-production imbalance, leading to a depletion of fracture pressure and intense water channeling.

(4) The simulation results for the depletion production of fixed-volume bottom water gas reservoirs demonstrate that when water saturation in fractures exceeds a critical threshold, there is a sudden decline in matrix gas supply due to the "water-sealed gas" phenomenon. Although continuous drainage and pressure reduction in fractures can partially alleviate water sealing and restore matrix gas supply, the enhancement in recovery is limited. Experiments under various production strategies show that higher gas production rates and larger water-to-gas volume ratios result in lower cumulative gas production before water sealing, higher abandonment pressure, greater difficulty in post-water-sealing recovery, and subsequently lower recovery.

(5) This study did not account for the effect of fracture closure due to increased effective stress following pore pressure depletion, which represents a limitation. Future work will aim to integrate stress-sensitive fracture models into the experimental setup.

CRediT authorship contribution statement

Yong-Liang Tang: Writing – review & editing, Resources, Project administration, Funding acquisition, Conceptualization. **Jun Yao:** Writing – review & editing, Project administration, Conceptualization. **Xue-Hao Pei:** Writing – original draft, Visualization, Methodology, Investigation, Data curation, Conceptualization. **Dong Chen:** Writing – review & editing, Methodology, Conceptualization. **Yong-Bin Zhang:** Writing – review & editing, Methodology, Conceptualization. **Feng-Lai Yang:** Writing – review & editing, Project administration, Conceptualization. **Xu Zhou:** Visualization, Methodology, Investigation. **Zhao-Qin Huang:** Writing – review & editing, Supervision, Conceptualization.

Declaration of competing interest

The authors declare that they have no known competing financial interests or personal relationships that could have appeared to influence the work reported in this paper.

Acknowledgments

This work was supported by the Major Science and Technology Projects of Xinjiang Uygur Autonomous Region (No. 2024A01010), Major Science and Technology Projects of China National Petroleum Corporation (No. 2023ZZ14YJ04) and the Youth Science and Technology Project of China National Petroleum Corporation (No. 2024DQ03061).

References

Ahmadi, P., Shahsavani, B., Malayeri, M., et al., 2019. Impact of different injection sites on the water and oil exchange in a fractured porous medium for different polymers: A visual study. J. Pet. Sci. Eng. 174, 948–958. https://doi.org/10.1016/j.petrol.2018.12.012.

Chen, D., Zhang, C., Yang, M., et al., 2024. Research on water invasion law and control measures for ultradeep, fractured, and low-porosity sandstone gas reservoirs: A case study of Kelasu gas reservoirs in Tarim Basin. Processes 12 (2), 310. https://doi.org/10.3390/pr12020310.

Du, Y., Mehmani, A., Xu, K., et al., 2020. Microfluidic diagnostics of the impact of local microfracture connectivity on hydrocarbon recovery following water injection. Water Resour. Res. 56, e2019WR026944. https://doi.org/10.1029/2019WR026944.

Fang, F., He, S., Zhuang, J., et al., 2024. Large-scale physical simulation experiment of water invasion law for multi-well development in sandstone gas reservoirs with strong water drive. Appl. Sci. 14 (17), 8067. https://doi.org/10.3390/app14178067.

Fang, F., Li, X., Gao, S., et al., 2016. Visual simulation experimental study on water invasion rules of gas reservoir with edge and bottom water. Nat. Gas Geosci. 27, 2246–2252. https://doi.org/10.11764/j.issn.1672-1926.2016.12.2246 (in Chinese).

Fang, F., Shen, W., Li, X., et al., 2019. Experimental study on water invasion mechanism of fractured carbonate gas reservoirs in Longwangmiao formation, Moxi block, Sichuan Basin. Environ. Earth Sci. 78, 316. https://doi.org/10.1007/s12665-019-8325-x.

Ge, L., Wang, J., Zhu, Z., et al., 2018. Three-dimensional physical simulation of enhanced oil recovery after water flooding for buried hill fractured reservoirs. China Offshore Oil Gas 30, 81–87. https://doi.org/10.11935/j.issn.1673-1506.2018.05.010 (in Chinese).

Guo, P., Zheng, J., Dong, C., et al., 2024. Invasion characteristics of marginal water under the control of high-permeability zones and its influence on the development of vertical heterogeneous gas reservoirs. Energies 17, 4724. https://doi.org/10.3390/en17184724.

Guo, X., Sun, L., Zhou, Y., et al., 2011. Large scale visual physical simulation experiment on water drive in fractured reservoir. Special Oil Gas Reservoirs 18, 109–111. https://doi.org/10.1016/S1003-9953(10)60145-4 (in Chinese).

Hu, Y., Li, X., Jiang, L., et al., 2022. Production experiment of multi-layer edge-water loose sandstone gas reservoir in Qaidam Basin. Nat. Gas Geosci. 33, 1499–1508. https://doi.org/10.11764/j.issn.1672-1926.2022.03.009 (in Chinese).

Huang, X., Guo, X., Zhou, X., et al., 2019. Effects of water invasion law on gas wells in high temperature and high pressure gas reservoir with a large accumulation of water-soluble gas. J. Nat. Gas Sci. Eng. 62, 68–78. https://doi.org/10.1016/j.jngse.2018.11.029.

Li, A., Zhang, D., Yao, J., et al., 2012. Physical simulation of water flooding in fractured-vuggy unit. Jcup 36, 130–135. https://doi.org/10.3969/j.issn.1673-5005.2012.02.022 (in Chinese).

Li, S., Liu, Y., Xue, L., et al., 2021. An investigation on water flooding performance and pattern of porous carbonate reservoirs with bottom water. J. Pet. Sci. Eng. 200, 108353. https://doi.org/10.1016/j.petrol.2021.108353.

Liu, H., Gao, S., Ye, L., et al., 2021. Change laws of water invasion performance in fractured–porous water-bearing gas reservoirs and key parameter calculation methods. Gas Ind. B. 8, 57–66. https://doi.org/10.3787/j.issn.1000-0976.2020.06.009.

Liu, Y., Ding, Z., Ao, K., et al., 2013. Manufacturing method of large-scale fractured porous media for experimental reservoir simulation. Soc. Petrol. Eng. J. 18, 1081–1091. https://doi.org/10.2118/163108-PA.

Liu, Y., Wang, S., Zhao, W., et al., 2023. Multi-dimensional experimental study of hydrocarbon gas-assisted gravity drainage. Arabian J. Sci. Eng. 48, 17031–17048. https://doi.org/10.1007/s13369-023-08333-3.

Shen, W., Li, X., Liu, X., et al., 2014. Physical simulation of water influx mechanism in fractured gas reservoirs. J Cent South Univ. 45, 3283–3287 (in Chinese).

Shoukry, A., Saraji, S., Piri, M., 2023. Two-phase displacement dynamics in fractured porous media of varying wettability states: A micromodel experimental investigation of matrix/fracture interactions. Adv. Water Resour. 176, 104447. https://doi.org/10.1016/j.advwatres.2023.104447.

Sun, K., Liu, H., Leung, J., et al., 2022. Investigation on water-drive performance of a fault-karst carbonate reservoir under different well patterns and injection-production modes based on 2D visualized physical models. J. Pet. Sci. Eng. 218, 110925. https://doi.org/10.1016/j.petrol.2022.110925.

Tang, H., Xu, S., Wang, X., et al., 2017. Water blocking damage of hyper-tight sandstone gas reservoir in Kelasu gas field. Fault-Block Oil Gas Field 24, 541–545. https://doi.org/10.6056/dkyqt201704023 (in Chinese).

Tong, K., Liu, H., Zhang, Y., et al., 2015. Three-dimensional physical modeling of waterflooding in metamorphic fractured reservoirs. Petrol. Explor. Dev. 42, 589–596. https://doi.org/10.1016/S1876-3804(15)30054-9.

Wang, J., Qi, X., Liu, H., et al., 2022. Mechanisms of remaining oil formation by water flooding and enhanced oil recovery by reversing water injection in fractured-vuggy reservoirs. Petrol. Explor. Dev. 49, 1110–1125. https://doi.org/10.1016/S1876-3804(22)60336-7.

Wang, J., Xu, Z., Liu, J., et al., 2024. Distribution rules of remaining oil by bottom water flooding and potential exploitation strategy in fault-controlled fractured-vuggy reservoirs. Petrol. Explor. Dev. 51, 1271–1286. https://doi.org/10.1016/S1876-3804(25)60540-4.

Wang, L., Yang, S., Liu, Y., et al., 2017. Experiments on gas supply capability of commingled production in a fracture-cavity carbonate gas reservoir. Petrol. Explor. Dev. 44, 824–833. https://doi.org/10.1016/S1876-3804(17)30093-9.

Wei, C., Zhang, C., Chen, D., et al., 2019. Seepage characteristics and development mechanism characterized by faults-fracture-pore “triple medium” in Keshen 2 gas reservoirs, Tarim Basin. Nat. Gas Geosci. 30, 1684–1693. https://doi.org/10.11764/j.issn.11672-1926.2019.07.011 (in Chinese).

Xu, X., Mei, Q., Chen, Y., et al., 2020. Experimental analysis method for water invasion and development performance of gas reservoir. Nat. Gas Geosci. 31, 1355–1366. https://doi.org/10.11764/j.issn.1672-1926.2020.08.004 (in Chinese).

Yang, D., Xie, K., Yin, Q., et al., 2024. Research status and prospect of water intrusion law in edge and bottom water gas reservoirs. Nat. Gas Geosci. 35, 1304–1322. https://doi.org/10.11764/j.issn.1672-1926.2024.01.014 (in Chinese).

Zhao, Y., Lu, G., Zhang, L., et al., 2020. Physical simulation of waterflooding development in large-scale fractured-vuggy reservoir considering filling characteristics. J. Pet. Sci. Eng. 191, 107328. https://doi.org/10.1016/j.petrol.2020.107328.

Zheng, W., Liu, Y., Liu, Z., et al., 2017. Physical simulation experimental study on low-permeability buried-hill fractured heavy oil reservoir. Pet. Geol. Recovery Effic. 24, 78–84. https://doi.org/10.13673/j.cnki.cn37-1359/te.2017.03.012 (in Chinese).

Zhong, J., Abedini, A., Xu, L., et al., 2018. Nanomodel visualization of fluid injections in tight formations. Nanoscale 10, 21994–22002. https://doi.org/10.1039/C8NR06937A.